Earth, Moon, and Planets (2022) 126:3
https://doi.org/10.1007/s11038-022-09545-7

The Distribution of Craters Within Craters

Anthony R. Dobrovolskis[1]

Received: 13 July 2021 / Accepted: 13 March 2022 / Published online: 23 March 2022

Abstract
The interior of a crater should have a lower mean areal density of smaller impact craters than nearby plains have, because the impacts are spread out over a larger surface area, and because the crater's wall partially shields its interior. Inside a crater shaped like a spherical bowl (a spherical cap turned upside-down), smaller primary impact craters should be spread uniformly, but secondary craters have a more complicated distribution, usually concentrated near the center. These results may help to distinguish between populations of primary and secondary craters, and should be of interest for interpreting counts of craters within craters.

Keywords Cratering · Geological processes · Impact processes

1 Introduction

Crater counting is a key tool in the arsenal of planetology. Many planets, moons, asteroids, comets, *etc.* are pocked to a greater or lesser extent with impact craters, whose areal density and distribution reveals much about the geologic and dynamical history of the target.

Impact craters come in two main types: primary and secondary. Primary craters are made by the impact of interplanetary objects, at speeds greater than the target's escape speed, and produce primary ejecta. Secondary craters are made by the re-impact of ejecta from primary craters, at speeds less than the target's escape speed, and produce secondary ejecta.

An intermediate type also has been described: Dobrovolskis and Lissauer (2004) originally dubbed them "poltorary" craters, after the Slavic word for "one and a half"; but Zahnle et al. (2008) re-labeled them "sesquinary", after the corresponding Latin term. Sesquinary craters are produced by impacts of circum-planetary debris on planets or their satellites, at speeds greater than the target's escape speed, but less than the speed of interplanetary bodies.

It is often difficult to distinguish among these types of craters. Sometimes primary and secondary craters can be distinguished by morphology; *e.g.*, ellipticity, depth/

✉ Anthony R. Dobrovolskis
anthony.r.dobrovolskis@nasa.gov

[1] SETI Institute, 245-3 NASA Ames Research Center, Moffett Field, Mountain View, CA 94035-1000, USA

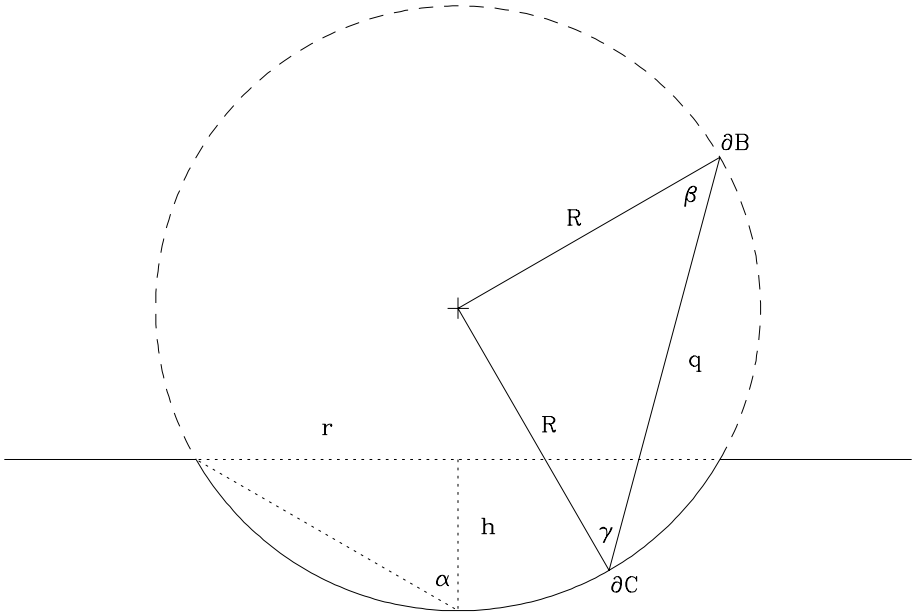

Fig. 1 Sketch of a crater shaped like a spherical bowl. Solid arc: interior of crater. Dashed arc: spherical bubble. Plus sign (+): center of bubble. Horizontal solid lines: plane of crater's rim. Horizontal dotted line: lid of crater

diameter ratios, rim sharpness, ejecta blankets, blocks, chains, rays, herringbone patterns, *etc.* (Melosh (1989)). This paper presents another criterion which may help to distinguish among the different crater populations.

This paper shows that the interior of a crater should have a lower density of smaller impact craters per unit area than nearby plains would have, because the impacts are spread out over a larger surface area, and because the crater's wall partially shields its interior. Inside a crater shaped like a spherical bowl (a spherical cap turned upside-down), smaller primary (and sesquinary) impact craters should be spread uniformly, but the distribution of secondary craters is more complicated, usually concentrated near the center. These results may help to distinguish between populations of primary and secondary craters, and should be of interest for interpreting counts of craters within craters.

The next section describes the cratering model used to obtain these results. Sect. 3 derives the distribution of primary craters inside a larger crater, while Sect. 4 derives its distribution of secondary craters. The final section briefly discusses the implications of these results.

2 Model

Consider a crater shaped like a spherical bowl, with rim radius r and depth h below the rim plane, as sketched in Fig. 1. Symbols are defined in Table 1. The surface area of the bowl's "lid" is then just πr^2, while the area of its interior is $\pi r^2 + \pi h^2$ (Ingersoll et al. (1992); see

Table 1 Symbols

∂B	Area element of bubble
∂C	Area element of crater's interior
c	Angular radius of ceiling
f	Angular radius of floor
G	Newton's constant of universal gravitation
g	Acceleration of gravity at the surface
h	Depth of crater below rim
L_P	Luminance of primary impactors
L_S	Luminance of secondary impactors
M	Mass of target body
$\hat{m}$	Unit vector along impact cone
$\hat{n}$	Upward unit normal to ∂C
P	Flux of primary impactors
P'	Rectified primary impact flux
P_0	Primary flux on a flat plain
p	Given by Formula (10)
q	Distance between ∂B and ∂C
R	Crater's radius of curvature
R_T	Radius of target body
r	Radius of crater's rim
S	Flux of secondary impactors
S'	Rectified secondary impact flux
S_0	Secondary flux on a flat plain
V	Launch speed or impact speed
V_C	V when Coriolis effects matter
V_E	Escape speed
x, y, z	Cartesian coordinates
α	Cone angle of rim from bottom of crater
β	Emission angle
γ	Impact angle
Δ	Horizontal distance traveled by ejecta
Δ_C	Δ when Coriolis effects matter
δ	Angular distance from bottom of crater
ζ	Cone angle of primary ejecta
θ	Co-latitude from the zenith
ρ	Angular radius of crater rim
ϕ	Azimuthal angle
ϕ_0	Given by Formula (9)
ω	Rotation rate of target body

also Appendix A of Dobrovolskis (2021)). For example, the interior area $2\pi r^2$ of a hemispherical crater ($h = r$) is twice the area πr^2 of its lid.

Assume also that this crater is horizontal, and that it lies on a convex region of the planet, moon, *etc.*, so that the rest of that body all lies below the plane of the crater's rim, and there is no "impact shadowing" from outside the crater. Then the flux of impactors through the crater's lid is the same as that on a nearby plain; but the impacts on the crater's

interior are spread over a greater area than its lid. Therefore, the interior of a crater has a lower mean density of smaller craters than nearby plains would have, by a factor of

$$\frac{\pi r^2 + \pi h^2}{\pi r^2} = 1 + h^2/r^2. \tag{1}$$

3 Primaries

This raises the question, how are these interior craters distributed? This section shows that primary impacts should be spread uniformly over the crater's interior. In order to demonstrate this, first complete the sphere by constructing a "bubble": a virtual geodesic dome or radome atop the crater's rim, with the same center and radius of curvature $R = (r^2 + h^2)/(2h) \geq r$ as the bowl, as shown by the dashed arc in Fig. 1.

Also assume that the incoming flux of primary (and sesquinary) impactors from space is isotropic (independent of direction). Note that this assumption is fair for sesquinary impactors, but poor for primary impacts on tidally locked satellites, which often show leading/trailing cratering asymmetries (*e.g.*, Horedt and Neukum (1984)).

When upward impactors (those originating below the horizon) are ignored, every area element ∂B of the bubble is exposed to the same impact flux; *i.e.*, the sky has a uniform radiance of primary impactors. Then by analogy with radiative transfer, each element ∂B of the bubble acts like a pinhole camera, and may be regarded as radiating downward impactors isotropically, and with equal impact luminance L_P (primary impactors per unit solid angle per unit area per unit time).

Each area element ∂C of the crater's interior receives an infinitesimal flux $\partial P = L_P \cos(\beta) \cos(\gamma) \partial B/q^2$ from every area element ∂B of the bubble, where β is the angle of emission from the normal to ∂B, γ is the angle of impact from the normal to ∂C, and q is the distance between ∂B and ∂C, as sketched in Fig. 1. By geometry, $\cos\beta = \cos\gamma = q/(2R)$ (Ingersoll et al. (1992)); so ∂P becomes just $L_P \partial B/(2R)^2$. Note that Fig. 1 is drawn for a vertical cross-section, but the above result applies for any area elements ∂B and ∂C.

It is possible to integrate ∂P over the surface area of the bubble; but it is simpler to notice that the above formula for ∂P is *independent* of the location of ∂C, so that every element of the crater's interior is exposed to the same flux from ∂B. Then the flux of primary impactors inside the bowl still must remain uniform when integrated over the bubble. If we assume that the efficiency of cratering is independent both of the impact angle γ[1], and also of the surface slope (perhaps plausible for small strength-dominated craters), then the density of primary craters inside the bowl must be uniform as well.

For example, consider a hemispheric crater of radius $r = h = R$, subject to a primary impact luminance L_P. Then each unit of area of the crater's lid is subject to a primary impact flux of $P_0 = \pi L_P$. This lid has an area of πr^2, so it intercepts $\pi r^2 P_0$ impactors per unit time; but these are spread out uniformly over an interior area of $2\pi r^2$, for an effective flux P of just $P_0/2$. As a simple check, an element ∂C of the crater's wall just below the rim is exposed to exactly half of the sky, while the lid and nearby plains see the whole sky.

[1] Zahnle et al. (2003) suggest that the diameter of a simple impact crater should be roughly proportional to the cube root of $\cos\gamma$.

As a more general check, consider the impact flux P at the very bottom of the crater. This point is exposed to a cone of sky with opening angle $\alpha = \text{Arctan}(r/h) = \text{Arcsin}(r/\sqrt{r^2 + h^2})$ (see Fig. 1). Because the sky (dotted semicircle in Fig. 1) has uniform primary impactor luminance L_P, integrating L_P over the solid angle of the sky cone gives

$$P = \oint_{-\pi}^{\pi} \int_0^{\alpha} L_P \sin(\theta) \cos(\theta) d\theta d\phi = \pi L_P [\sin^2 \theta]_0^{\alpha} = \pi L_P \sin^2 \alpha = \frac{\pi L_P}{1 + h^2/r^2}, \quad (2)$$

where ϕ is azimuth and θ is co-latitude from the zenith.

In the limit $h = 0$, Formula (2) above reduces to $P = \pi L_P$, the classic result for a flat plain. For a hemisphere ($h = r$), Formula (2) gives $P = \pi L_P/2$, as derived above. In fact, Formula (2) gives the same result as Formula (1) for all depth/radius ratios; and it applies over the entire interior of the crater, not just at its bottom.

4 Secondaries

Like primary and sesquinary craters, secondaries should have a lower areal density inside larger craters than on nearby plains. Unlike primaries and sesquinaries, though, secondaries should not be distributed uniformly. This section derives an approximate distribution of secondary craters inside larger craters.

Secondary impacts differ from primary (and sesquinary) impacts not only in their impact speed, but also in their impact angles. The vast majority of ejecta from primary impacts are launched in a narrow cone typically $\sim 45°$ from the normal to the surface. However, some variations of this angle do occur; for example, see Anderson et al. (2004) and Luther et al. (2018). Thus for greater generality, henceforth I will use ζ as the angle of launch from the vertical.

On a spherical target of radius R_T and mass M, primary ejecta with launch speeds V less than the escape speed $V_E = \sqrt{2GM/R_T}$ promptly return to its surface (or re-enter its atmosphere) as secondary impacts at the same speed V as their launch speed; *and with impact angles equal to their launch angles* ζ, as long as Coriolis effects are unimportant.

4.1 Coriolis effects

From Dobrovolskis (1981), for launch angles near 45°, Coriolis effects seem to be unimportant when

$$V < V_C \approx 0.2\ g/\omega\ ; \quad (3)$$

or in terms of the range Δ (the horizontal distance traveled by the ejecta),[2] when

$$\Delta < \Delta_C = V_C^2/g \approx 0.04\ g/\omega^2, \quad (4)$$

at least over the hemisphere centered on the impact. Here g is the surface gravity of the target body, and ω is its rotation rate.

[2] In Dobrovolskis (1981), I forgot to mention that Formula (8) for the range implies $\sin(\Delta/2) = v_h v_z/e$. In the near-field limit, when the horizontal and vertical components v_h and v_z of the launch velocity both are much less than the escape speed, this reduces to the classic result $\Delta = 2v_h v_z/g$ on a flat planet.

Table 2 Parameters for selected bodies

Planet or moon	Radius R_T (km)	Escape speed V_E (km/s)	Surface gravity g (m/s^2)	Current rotation rate ω (10^{-6}rad/s)	V_C (km/s)	Δ_C (km)
Mercury	2 440	4.25	3.70	1.24	600	96×10^6
Earth	6 371	11.19	9.81	72.9	27	74 000
Moon	1 737	2.83	1.62	2.66	120	9.2×10^6
Mars	3390	5.03	3.72	70.9	11	30 000
Ceres	470	0.516	0.284	192	0.30	310
Ganymede	2 634	2.74	1.43	10.2	28	20 000
Callisto	2 410	2.44	1.24	4.36	57	2.6×10^6
Mimas	198	0.159	0.0637	77.2	0.17	430
Enceladus	252	0.239	0.113	53.1	0.43	1 600
Tethys	531	0.394	0.146	38.5	0.76	3 900
Dione	561	0.510	0.232	26.6	1.7	12 000
Rhea	764	0.635	0.264	16.1	3.3	41 000
Miranda	236	0.193	0.079	51.4	0.31	1 200
Ariel	579	0.559	0.269	28.9	1.9	13 000
Umbriel	585	0.539	0.249	17.5	2.8	33 000
Titania	788	0.773	0.379	8.35	9.1	220 000
Oberon	761	0.727	0.346	5.40	13	470 000
Triton	1 353	1.46	0.779	12.4	13	200 000
Pluto	1 188	1.21	0.620	11.4	11	190 000
Charon	606	0.591	0.288	11.4	5.1	89 000

Table 2 lists the above parameters for selected near-spherical bodies of interest, along with their radii R_T and escape speeds V_E, for comparison. Note that $g = GM/R_T^2 = V_E^2/(2R_T)$, where G is Newton's constant of universal gravitation.

Of all 20 bodies listed in Table 2, only the rapidly rotating dwarf planet Ceres, with a spin period of $2\pi/\omega \approx 9.074$ hours, has V_C and Δ_C slightly less than its escape speed V_E and its mean radius R_T, respectively. Thus Ceres' secondary ejecta may be somewhat influenced by Coriolis effects, as indeed found by (Schulzeck et al. (2017, 2018)). All of the other tabulated moons and planets have $V_C > V_E$ and $\Delta_C > R_T$, so their secondary ejecta should not be significantly influenced by Coriolis effects.

4.2 Crater classes

Henceforth I shall neglect Coriolis effects, and assume that every surface element of the target body is exposed to an intermittent hail of non-local primary ejecta incoming at an angle of ζ with respect to the vertical. To illustrate, Fig. 2 again shows a crater shaped like a spherical bowl, but now the area element ∂C of its interior receives a flux of secondary impacts along a cone of opening angle ζ (drawn as 45° here) with respect to the vertical.

Figure 2 is drawn for the special case when the impact cone is just tangent to the rim of the crater. In this case, the level of the area element ∂C defines the "floor line" of the crater. I call the portion of the crater below this floor line the "floor", and the portion of the crater above the floor line the "wall". Then surface elements of the floor are fully exposed to the

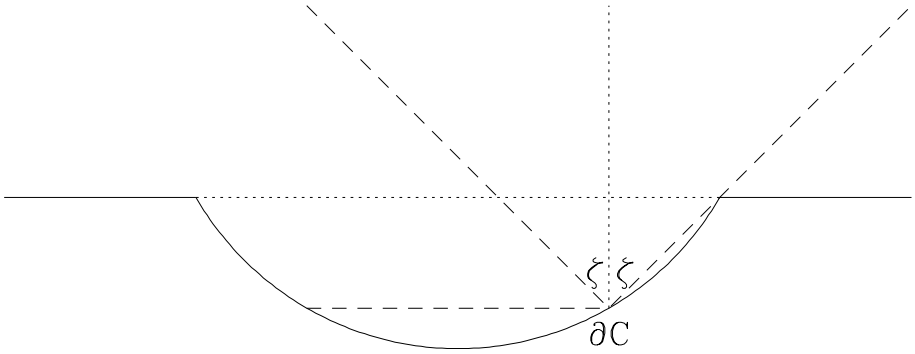

Fig. 2 Sketch of a Deep crater shaped like a spherical bowl. Solid arc: interior of crater. Horizontal solid lines: plane of crater's rim. Horizontal dotted line: lid of crater. Vertical dotted line: axis of impact cone. Diagonal dashed lines: impact cone. Horizontal dashed line: floor level

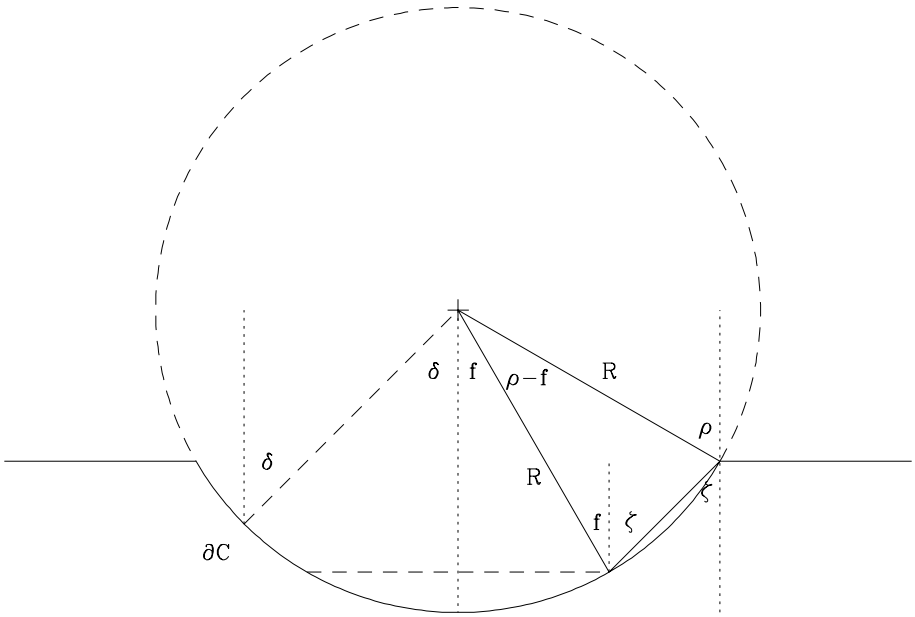

Fig. 3 Sketch of a Deep crater shaped like a spherical bowl. Solid arc: interior of crater. Dashed arc: spherical bubble. Plus sign (+): center of bubble. Horizontal solid lines: plane of crater's rim. Horizontal dashed line: floor level. Dotted lines are vertical

flux of primary ejecta; but to belabor the radiative analogy, surface elements of the wall are partially "shaded" from the primary ejecta by the crater wall itself.

Figure 3 shows the same bowl-shaped crater again, where now δ is defined as the angular distance of the area element ∂C from the bottom of the crater, as measured from the center of the bubble; note that δ is also the slope of ∂C with respect to the horizontal. Likewise, ρ is the angular radius of the crater's rim as well as the slope there, while $|f|$ is both the angular radius and the slope of its floor line.

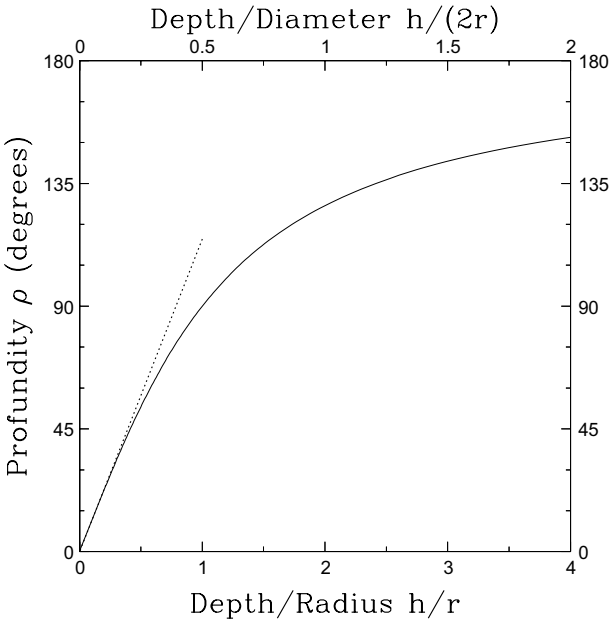

Fig. 4 Solid curve: Relation between a crater's profundity ρ and its depth/radius ratio h/r, or its depth/diameter ratio $h/(2r)$. Dotted line: Approximation $h/r \approx \rho/114.6°$

Note that the angular radius ρ is a measure of a crater's shape rather than its size; it might be called the crater's "profundity". Note also that $\sin\rho = r/R = 2rh/(r^2 + h^2)$, $\cos\rho = (R - h)/R = (r^2 - h^2)/(r^2 + h^2)$, $\tan\rho = 2rh/(r^2 - h^2)$, and

$$h/r = (1 - \cos\rho)/\sin\rho = \sin(\rho)/(1 + \cos\rho). \tag{5}$$

Figure 4 graphs relation (5) above between a crater's profundity ρ and its depth/radius ratio h/r, or its depth/diameter ratio $h/(2r)$. Thus, for example, $h/r = 0$ when $\rho = 0$, $h/r = \sqrt{2} - 1 \approx 0.414$ when $\rho = 45°$, $h/r = 1$ when $\rho = 90°$, $h/r = \sqrt{2} + 1 \approx 2.414$ when $\rho = 135°$, and h/r approaches infinity as ρ approaches 180°.

The solid isosceles triangle in Fig. 3 shows that

$$180° = \rho + f + 2\zeta \;\Leftrightarrow\; f = 180° - 2\zeta - \rho \approx 90° - \rho, \tag{6}$$

provided that $0 < f < \rho$; this is equivalent to $90° - \zeta \approx 45° < \rho < 180° - 2\zeta \approx 90°$. In this case, the crater has both a wall and a floor, as in Fig. 3; I call such craters "Deep". However, if $f > \rho$, then $\rho < 90° - \zeta \approx 45°$, the crater wall vanishes, and its whole interior becomes floor, fully exposed to primary ejecta; I call such craters "Shallow". For Shallow craters, $h/r \approx \rho\pi/360° \approx \rho/114.6°$, as graphed by the dotted line in Fig. 4.

On the contrary, if $\rho > 180° - 2\zeta \approx 90°$, then f turns out to be negative. In this case, the entire floor is shielded from primary ejecta ! In addition, if $\rho > 90° + \zeta \approx 135°$, the uppermost portions of the crater also are completely shielded from primary ejecta, as sketched in Fig. 5. Pursuing the architectural analogy further, I define $c \equiv 180° + 2\zeta - \rho \approx 270° - \rho$ as the "ceiling line", and the portion of the crater above this level as the "ceiling". The floor and ceiling of the crater in Fig. 5 are denoted by the thick arcs.

I call craters with $180° - 2\zeta < \rho < 90° + \zeta$ "Profound", for lack of a better term, and those with $\rho > 90° + \zeta$ "Cavernous", although such cavities hardly deserve the name of

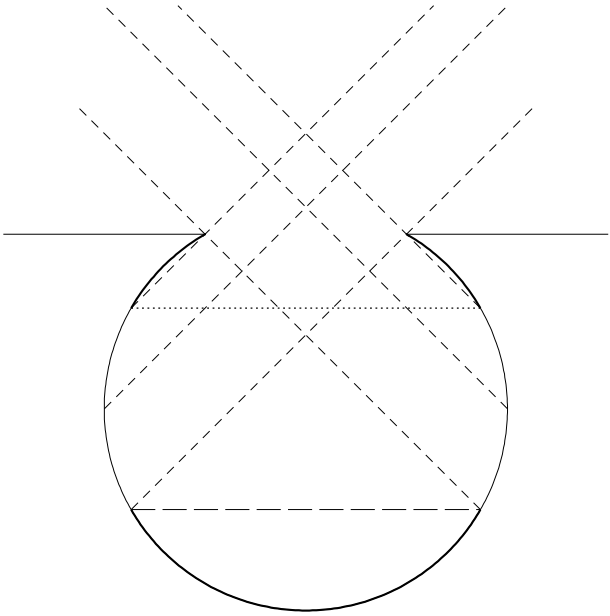

Fig. 5 Sketch of a Cavernous crater shaped like a spherical bowl. Solid arc: interior of crater. Thick arcs: floor and ceiling of crater. Horizontal solid lines: plane of crater's rim. Horizontal dashed line: floor level. Horizontal dotted line: ceiling level. Diagonal dashed lines: trajectories of incoming primary ejecta

"craters"; they would resemble the "skylights" seen on the Moon and Mars (*e.g.*, Cushing et al. (2007)), while their lids resemble the oculus of a dome such as the Pantheon in Rome.

In terms of a crater's depth h below its rim of radius r, Cavernous craters have $h/r > (1+\sin\zeta)/\cos\zeta$, Profound craters have $(1+\cos(2\zeta))/\sin(2\zeta) < h/r < (1+\sin\zeta)/\cos\zeta$, Deep craters have $(1-\sin\zeta)/\cos\zeta < h/r < (1+\cos(2\zeta))/\sin(2\zeta)$, and Shallow craters have $h/r < (1-\sin\zeta)/\cos\zeta$. If we set $\zeta = 45°$, then Cavernous craters have $h/r > \sqrt{2}+1 \approx 2.414$, Profound craters have $1 < h/r < \sqrt{2}+1 \approx 2.414$, Deep craters have $0.414 \approx \sqrt{2}-1 < h/r < 1$, and Shallow craters have $h/r < \sqrt{2}-1 \approx 0.414$. By this standard, most measured craters on moons and planets are Shallow.

4.3 Floor

Although the floor of a profound or cavernous crater receives no secondary impacts, an area element ∂C on the floor of a Shallow or Deep crater is exposed to a flux of secondary ejecta

$$S = \oint_{-\pi}^{\pi} L_S \cos(\gamma) d\phi, \tag{7}$$

where ϕ is the azimuthal angle around the impact cone. Note that L_S in Formula (7) above is a one-dimensional impact luminance (*i.e.*, secondary impactors per unit angle per unit area per unit time), rather than two-dimensional, like the primary impact luminance L_P.

In order to evaluate the impact angle γ, I define a right-handed Cartesian coordinate system x, y, z, originating at the center of the bubble, with corresponding unit vectors $\hat{x}, \hat{y}, \hat{z}$, such that $\hat{z}$ points straight upwards. Now without loss of generality, consider an

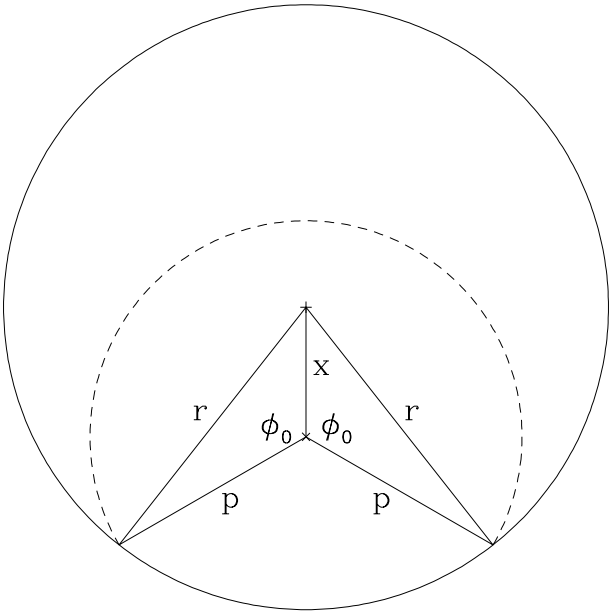

Fig. 6 Lid of a bowl-shaped crater. Solid circle: crater rim. Dashed arc: intersection of secondary impact cone with lid. This is drawn for the convenient triplet of $x = 6$, $p = 10$, and $r = 14$, so that $\phi_0 = 120°$; then $R = \sqrt{205} \approx 14.318$ if $\zeta = 45°$

area element ∂C of the crater floor, lying at $(x, 0, z) = (R \sin\delta, 0, -R\cos\delta)$. Then the unit vector normal to ∂C in the upward direction is $\hat{n} = \hat{z}\cos(\delta) - \hat{x}\sin\delta$.

For convenience, let $\phi = \pi$ in the direction of $\hat{x}$, so that the unit vector $\hat{m}$ along the impact cone can be written $\hat{m} = \hat{z}\cos(\zeta) - [\hat{x}\cos(\phi) + \hat{y}\sin\phi]\sin\zeta$. Then $\cos\gamma = \hat{m} \bullet \hat{n}$, and Formula (7) becomes

$$\begin{aligned} S &= L_S \oint_{-\pi}^{\pi} [\hat{m} \bullet \hat{n}] d\phi = L_S \oint_{-\pi}^{\pi} [\cos(\zeta)\cos(\delta) + \cos(\phi)\sin(\zeta)\sin\delta] d\phi \\ &= 2\pi L_S \cos(\zeta)\cos\delta = S_0 \cos\delta. \end{aligned} \tag{8}$$

Here $S_0 \equiv 2\pi L_S \cos\zeta$ is the flux of secondary impacts at any point of the crater's lid, or on a nearby plain.

4.4 Wall

Although Formula (8) above for the secondary flux on the floor of a crater is rather simple, the result for crater walls is more complicated, because of impact shadowing. This may best be visualized by considering the intersection of the crater's lid with the impact cone having its apex at an area element ∂C of the wall, as sketched by the dashed arc of radius p in Fig. 6. Here the solid circle of radius r represents the rim of the crater, while x is the distance between the vertical symmetry axes of the impact cone and of the crater itself.

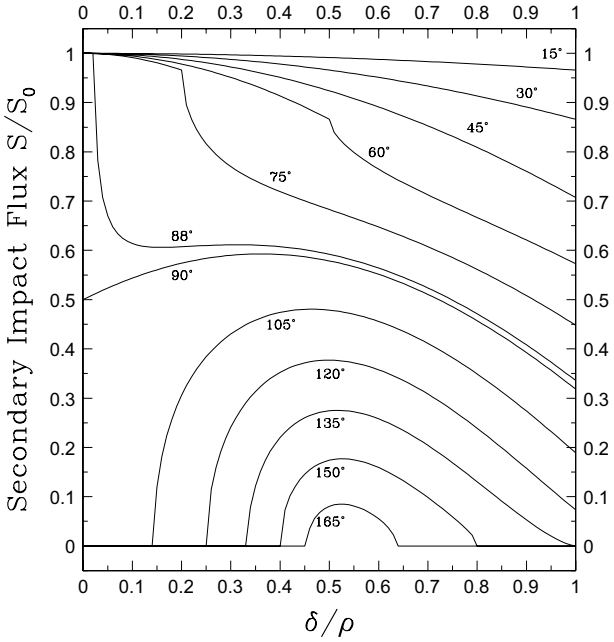

Fig. 7 The flux S of secondary impactors (normalized by the secondary flux S_0 on a flat plain) as a function of the angular distance δ from the bottom of a crater of angular radius ρ

Note that the dashed arc is no longer a complete circle, as it was for area elements of the floor. Therefore the complete loop integral from $-\pi$ to π in Formula (8) for the secondary flux at ∂C must be replaced by an integral from $-\phi_0$ to ϕ_0:

$$S = L_S \int_{-\phi_0}^{\phi_0} [\cos(\zeta)\cos(\delta) + \cos(\phi)\sin(\zeta)\sin\delta] d\phi$$
$$= 2L_s[\phi_0 \cos(\zeta)\cos(\delta) + 2\sin(\phi_0)\sin(\zeta)\sin\delta] = S_0[\cos(\delta)\phi_0 + \sin(\delta)\tan(\zeta)\sin\phi_0]/\pi. \tag{9}$$

Note how Formula (9) above reduces to Formula (8) on the floor of a crater, where $\phi_0 = \pi$.

From the Law of Cosines,

$$r^2 = x^2 + p^2 - 2xp\cos\phi_0 \;\Leftrightarrow\; \cos\phi_0 = \frac{x^2 + p^2 - r^2}{2xp}; \tag{10}$$

while from simple trigonometry,

$$p = [h - z - R]\tan\zeta. \tag{11}$$

4.5 Distribution

Figure 7 graphs the impact impact flux S of primary ejecta (normalized by S_0) inside a crater shaped like a spherical bowl, from Formulae (8) and (9), as a function of the angular distance δ (normalized by ρ) for several values of the crater's angular radius ρ, as labeled. This figure is drawn for an impact angle of $\zeta = 45°$ from the vertical.

The curves for $\rho = 45°$, 30°, and 15° all lie in the Shallow regime, where the interior of the crater is all floor, fully exposed to the flux of primary ejecta. In the limiting case $\rho = 0$ of a completely flat "crater", $S = S_0$ everywhere.

The curves for $\rho = 60°$, 75°, and 88° all correspond to Deep craters, with both a fully exposed floor and a partially shielded wall. Note how S drops abruptly (continuously but non-differentiably) at the floor level between the floor and wall.

For $\rho <\sim 88°$, S decreases monotonically with increasing δ; but in the narrow range $88° < \rho < 90°$, S has one local minimum and one local maximum on the crater wall. The curve for $\rho = 90°$, representing a hemispheric crater, is $S/S_0 = \sin(\delta)/\pi + \cos(\delta)/2$; this reaches a single peak of $S/S_0 = (\pi/2 + 2/\pi)/\sqrt{4 + \pi^2} \approx 0.5927$ at $\delta = \arctan(2/\pi) \approx 32.48°$ ($\delta/\rho \approx 0.3609$).

The curves for $\rho = 105°$, 120°, and 135° correspond to Profound craters, with a floor fully shielded from primary ejecta ($S = 0$). The curves for $\rho = 150°$ and 165° correspond to Cavernous craters, with a ceiling as well as a floor, both fully shielded from secondary impacts.

In both Profound and Cavernous craters, note how S reaches a single peak partway up the crater wall. In the limiting case $\rho = 180°$ of a spherical cavity with a pinhole opening at the very top, the floor and ceiling meet at $\delta = 2\zeta \approx 90°$, so the entire cavity is shielded from primary ejecta, and S vanishes everywhere.

The left-hand axis of Fig. 7 ($\delta = 0$) represents the very bottom of the crater. In Shallow and Deep craters ($\rho < 90°$), this point is fully exposed to primary ejecta, so $S = S_0$ there; but in Profound and Cavernous craters ($\rho > 90°$), this point is fully shielded from primary ejecta, so S vanishes there.

The right-hand edge of Fig. 7 ($\delta = \rho$) represents points just below the rim of the crater. Here S vanishes for all Cavernous craters, but reduces to $S_0 \cos\rho$ for Shallow craters. For Deep and Profound craters, Formula (8) for S is not simple, but Formula (9) approaches the limit $\cos\phi_0 = -\cos(\rho)\cos(\zeta)/[\sin(\rho)\sin\zeta] \approx -\cos(\rho)/\sin\rho$ for a plane with slope ρ.

4.6 Rectification

The angular radius ρ of a crater and the angular distance δ from its bottom are unfamiliar constructs, and may be inconvenient for many purposes. For most work on craters, more convenient parameters include a crater's radius r or diameter $2r$, its depth h, and the horizontal distance x from its center. Note that $x = r\sin\delta$, and $\delta = \mathrm{Arcsin}(x/r)$.

Furthermore, craters are often viewed from near the zenith, and most mapping and crater counting is done in plan view, projecting all features onto a horizontal plane (or sphere). So it is of interest to consider the density of small craters inside a larger crater in plan view, in terms of r, h, and x.

When projected vertically, the density of craters is amplified by the secant of the local slope. The following considers only Shallow or Deep craters with $\rho \le 90°$, so the slope is δ, and its secant is $1/\cos\delta = 1/\sqrt{1 - x^2/r^2}$. Then the rectified density of primary craters is just proportional to their rectified impact flux $P' \equiv P/\cos\delta = P/\sqrt{1 - x^2/r^2}$.

Likewise, the rectified density of secondary craters is proportional to their rectified impact flux $S' \equiv S/\cos\delta$. Dividing Formula (8) for the floor of a Shallow or Deep crater by $\cos\delta$ gives just the constant $S' = S_0$, the same as the secondary flux on a nearby plain. In contrast, dividing Formula (9) for the wall of a Deep crater by $\cos\delta$ gives the more complicated formula

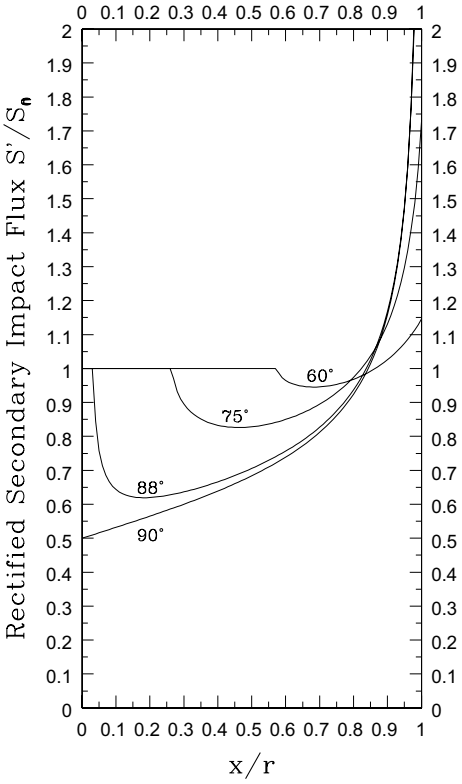

Fig. 8 The rectified flux S' of secondary impactors (normalized by the secondary flux S_0 on a flat plain) as a function of the horizontal distance x from the center of a Deep crater of radius r. Each curve is labeled with the crater's angular radius ρ

$$S' = S_0[\phi_0 + \tan(\delta)\tan(\zeta)\sin\phi_0]/\pi. \tag{12}$$

Again, note how Formula (12) above reduces to Formula (11) on the floor of a crater, where $\phi_0 = \pi$.

Figure 8 graphs the rectified impact flux S' of primary ejecta inside Deep craters from Formula (12), for $\zeta = 45°$. As in Fig. 7, curves are labeled with the crater's angular radius ρ; recall that $h/r = \sin(\rho)/(1+\cos\rho)$. The curve labeled 90° for a hemispheric crater ($h = r = R$, $\phi_0 = \pi/2$) is $S'/S_0 = 1/2 + \tan(\delta)/\pi = 1/2 + (x/r)[1-(x/r)^2]^{-1/2}/\pi$. This curve actually crosses the curve for $\rho = 88°$ at $x/r \approx 0.965$, $S'/S_0 \approx 1.685$; but the upper halves of both curves are almost indistinguishable in Fig. 8.

As Fig. 8 shows, projecting the secondary crater density onto the horizontal renders S' completely uniform on the entire floor of the crater. On the crater's wall, S' first drops because of the shielding effect, but then rises with secant(δ). Inside Shallow craters ($\rho < 90° - \zeta \approx 45°$), $S' = S_0$ everywhere.

5 Discussion

We have seen that the density S of secondary craters inside Shallow and Deep bowl-shaped craters decreases nearly monotonically with distance from the center, but their rectified density S' is uniform over the crater floor. In contrast, the density P of primary (and sesquinary) craters inside any bowl-shaped crater is uniform; but their rectified density P' increases

monotonically with distance from the center. In principle, this may provide a statistical means of distinguishing primary and secondary crater populations.

There are several obstacles to this application, though. Most glaringly, most craters are not shaped like ideal spherical bowls or woks; many resemble skillets or frying pans instead. This can be due to a variety of effects, including slumping of walls, isostatic rebound of floors, flooding by lava, and infilling by ejecta.

Another questionable assumption is that the primary impact flux is isotropic. Leading/trailing asymmetries contribute to this effect on tidally locked moons (*e.g.*, Horedt and Neukum (1984)), but gravitational focussing does not.

Conversely, another dubious assumption is that all ejecta from primary craters are launched at a unique zenith angle ζ. In fact, their launch angles span range of zenith angles; this could smear the distribution of secondary craters inside craters, and reduce its statistical contrast with the distribution of primaries.

A subtler difficulty concerns the level of crater saturation. When the density of craters is so great that they begin to obliterate one another (usually at the smallest sizes), crater counts underestimate the impact flux. This may obscure the true distribution of impacts, and might also complicate its interpretation.

Most of the above diffuculties may be treatable, with the possible exception of slumping at higher slope angles. If so, this approach may provide a new tool for interpreting crater counts.

Acknowledgements I thank Kevin Zahnle and Jack Lissauer for previewing the manuscript, and Greg Michael and Jamie Gilmour for reviewing it.

References

J.L.B. Anderson, P.H. Schultz, J.T. Heinek, Experimental ejection angles for oblique impacts: Implications for the subsurface flow-field. Meteorit. Planet. Sci. **39**, 303–320 (2004)

G.E. Cushing, T.N. Titus, J.J. Wynne, P. Christensen, THEMIS observes possible cave skylights on Mars. Geophys. Res. Lett. **34**, L17201 (2007)

A. Dobrovolskis, Ejecta patterns diagnostic of planetary rotations. Icarus **47**, 203–219 (1981)

A.R. Dobrovolskis, J.J. Lissauer, The fate of ejecta from Hyperion. Icarus **169**, 462–473 (2004)

A.R. Dobrovolskis, Surface potential of a rotating duplex consisting of two conjoined spheres. Icarus **358**, 114061 (2021)

G.P. Horedt, G. Neukum, Cratering rate over the surface of a synchronous satellite. Icarus **60**, 710–717 (1984)

A.P. Ingersoll, T. Svitek, B.C. Murray, Stability of polar frosts in spherical bowl-shaped craters on the Moon, Mercury, and Mars. Icarus **100**, 40–47 (1992)

R. Luther, M.-H. Zua, G. Collins, K. Wünnemann, Effect of target properties and impact velocity on ejection dynamics and ejecta deposition. Meteorit. Planet. Sci. **53**, 1705–1732 (2018)

H.J. Melosh, *Impact Cratering: A Geologic Process* (Oxford Univ. Press, New York, 1989)

F. Schulzeck, N. Schmedemann, S. Schröder, U. Carsenty, R. Jaumann, K. Stephan, C. A. Raymond, C. T. Russell, Ejecta pattern and velocities of a boulder crater on Ceres. LPSC **XLVIII**, abstract 1387 (2017)

F. Schulzeck, S.E. Schroöder, N. Schmedemann, K. Stephan, R. Jauman, C.A. Raymond, C.T. Russell, Global and local re-impact and velocity regime of ballistic ejecta of boulder craters on Ceres. Planet. Space Sci. **153**, 142–156 (2018)

K. Zahnle, P. Schenk, H. Levison, L. Dones, Cratering rates in the outer solar system. Icarus **163**, 263–289 (2003)

K. Zahnle, J.L. Alvarellos, A. Dobrovolskis, P. Hamill, Secondary and sesquinary craters on Europa. Icarus **194**, 660–674 (2008)